The Mass Spectrum Analyzer (MSA) on board the BepiColombo MMO

Dominique C. Delcourt, Y. Saito, Frédéric Leblanc, Christophe Verdeil, S. Yokota, M. Fraenz, H. Fischer, B. Fiethe, Bruno Katra, Dominique Fontaine, et al.

AGU PUBLICATIONS

JGR

Journal of Geophysical Research: Space Physics

TECHNICAL REPORTS: METHODS

10.1002/2016JA022380

Special Section:
Measurement Techniques in Solar and Space Physics: Particles

Key Points:
- The MSA instrument of BepiColombo MMO will measure three-dimensional mass-resolved ion distribution functions in Hermean magnetosphere
- Thanks to seldom flown reflectron technique that is used for measuring time of flights, mass resolution is greatly enhanced (m/Dm > 40)
- Measurements with high time resolution (about MMO spin period) will allow detailed analysis of the dynamics of ions of planetary origin

Correspondence to:
D. Delcourt,
dominique.delcourt@lpp.polytechnique.fr

Citation:
Delcourt, D., et al. (2016), The Mass Spectrum Analyzer (MSA) on board the BepiColombo MMO, *J. Geophys. Res. Space Physics*, *121*, 6749–6762, doi:10.1002/2016JA022380.

Received 13 JAN 2016
Accepted 10 JUN 2016
Accepted article online 17 JUN 2016
Published online 4 JUL 2016
Corrected 16 JUL 2016

This article was corrected on 16 JUL 2016. See the end of the full text for details.

The Mass Spectrum Analyzer (MSA) on board the BepiColombo MMO

D. Delcourt[1], Y. Saito[2], F. Leblanc[1], C. Verdeil[1], S. Yokota[2], M. Fraenz[3], H. Fischer[3], B. Fiethe[4], B. Katra[1], D. Fontaine[1], J.-M. Illiano[1], J.-J. Berthelier[5], N. Krupp[3], U. Buhrke[3], F. Bubenhagen[4], and H. Michalik[4]

[1]LPP-CNRS-UPMC, Paris, France, [2]ISAS-JAXA, Sagamihara, Japan, [3]MPS, Göttingen, Germany, [4]IDA, Braunschweig, Germany, [5]LATMOS-IPSL, Paris, France

Abstract Observations from the MESSENGER spacecraft have considerably enhanced our understanding of the plasma environment at Mercury. In particular, measurements from the Fast Imaging Plasma Spectrometer provide evidences of a variety of ion species of planetary origin (He^+, O^+, and Na^+) in the northern dayside cusp and in the nightside plasma sheet. A more comprehensive view of Mercury's plasma environment will be provided by the BepiColombo mission that will be launched in 2018. On board the BepiColombo MMO spacecraft, the Mercury Plasma/Particle Experiment consortium gathers different sensors dedicated to particle measurements. Among these sensors, the Mass Spectrum Analyzer (MSA) is the instrument dedicated to plasma composition analysis. It consists of a top hat for energy analysis followed by a time-of-flight (TOF) chamber to derive the ion mass. Taking advantage of the spacecraft rotation, MSA will measure three-dimensional distribution functions in one spin (4 s), from energies characteristic of exospheric populations (in the eV range) up to plasma sheet energies (up to ~38 keV/q). A notable feature of the MSA instrument is that the TOF chamber is polarized with a linear electric field that leads to isochronous TOFs and enhanced mass resolution (typically, $m/\Delta m \approx 40$ for ions with energies up to 13 keV/q). At Mercury, this capability is of paramount importance to thoroughly characterize the wide variety of ion species originating from the planet surface. It is thus anticipated that MSA will provide unprecedented information on ion populations in the Hermean environment and hence improve our understanding of the coupling processes at work.

1. Introduction

Since the Mariner 10 flybys in 1974–1975, it is known that planet Mercury possesses an intrinsic though reduced magnetic field that leads to the formation of a magnetosphere with spatial and temporal scales much smaller than those at Earth (by about a factor 8 and a factor 40, respectively). More recently, during more than 4 years (from orbit insertion in March 2011 to final operations in April 2015), the MESSENGER mission provided a wealth of observations of the planet and its ionized and neutral particle environments. As far as plasma is concerned, the MESSENGER payload featured a limited set of sensors, viz., an ion mass spectrometer (Fast Imaging Plasma Spectrometer (FIPS)) and an energetic particle analyzer (Energetic Particle Spectrometer) [e.g., *Andrews et al*., 2007], together with a magnetometer (MAG) [e.g., *Anderson et al*., 2007]. The MESSENGER observations include the confirmation of an intrinsic magnetic field that is somewhat shifted northward (by about 480 km) [e.g., *Anderson et al*., 2011] as well as sporadic injections of energetic electrons as observed by Mariner 10 [e.g., *Ho et al*., 2011]. MESSENGER also revealed that Mercury's magnetosphere is highly dynamical with, e.g., recurrent flux transfer [e.g., *Slavin et al*., 2012] or dipolarization events [e.g., *Sundberg et al*., 2012] on time scales of seconds. MESSENGER also provided evidences of planetary ions in various regions of the Hermean magnetosphere [e.g., *Zurbuchen et al*., 2008, 2011; *Raines et al*., 2013, 2015]. An example is given in Figure 1 adapted from *Raines et al*. [2013] that shows color-coded densities of Na^+ and O^+ ions as a function of altitude and local time. In this figure, a density peak is particularly noticeable between ~1000 km and ~6000 km altitude in the equatorial premidnight sector that can be interpreted as the result of tailward transport of material ejected from the high-latitude dayside cusp [*Delcourt*, 2013].

The BepiColombo mission that is now scheduled for launch in 2018 and arrival at Mercury in 2024 will significantly expand our understanding of Mercury and its environment with a more comprehensive instrumentation than that of MESSENGER and with an innovative flight plan. BepiColombo consists of two spacecraft, one (MPO) led by European Space Agency (ESA) and dedicated to planetary studies and the other (MMO) led by Japan Aerospace Exploration Agency (JAXA) and dedicated to analysis of the Hermean environment. This latter spacecraft is spin stabilized (with spin period of 4 s and spin axis perpendicular to the ecliptic plane) along a polar orbit of 590 km × 11,640 km (with orbital period of 9.3 h). This will allow in particular thorough investigation

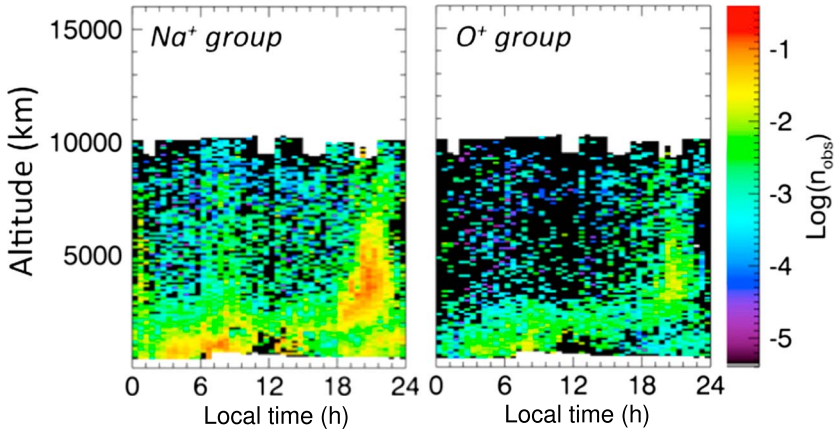

Figure 1. Densities of (left) Na^+ group and (right) O^+ group ions as measured by the FIPS instrument on board MESSENGER. Densities are shown as a function of local time and altitude and coded according to the color scale at right (from *Delcourt* [2013]).

of Mercury's magnetotail at various distances, including the presumed region where the near-Mercury neutral line forms (within a few planetary radii). The payload of the MMO spacecraft includes an extensive instrumental suite for space plasma study. In particular, for the first time, MMO will allow for measurements of thermal electrons, electric field, and plasma waves, and it will thus provide a unique unprecedented view of Mercury's magnetized environment.

The Mercury Plasma/Particle Experiment (MPPE) consortium on board the MMO consists of seven sensors for plasma, high-energy particle, and energetic neutral atom measurements with sufficiently high time resolution, wide energy range, wide dynamical range, and wide angular coverage, taking advantage of the spacecraft rotation [*Saito et al*., 2010]. Among these MPPE sensors, the Mass Spectrum Analyzer (MSA) is a time-of-flight spectrometer that will provide information on plasma composition and ion distribution functions [*Delcourt et al*., 2009]. In contrast to the Earth's magnetosphere, a wide variety of ion species up to large mass-to-charge ratios (e.g., K^+ and Ca^+) are expected in the magnetosphere of Mercury as a result of the direct interaction of the solar wind with the planet surface. Due to the limited mass resolution of the FIPS instrument on board the MESSENGER, it was not possible to precisely resolve these different ion species which have been classified according to coarse mass groups, as displayed for instance in Figure 1 that is adapted from *Raines et al*. [2013]. Because of its enhanced (reflectron-type) mass resolution capability together with its three-dimensional field of view, the MSA instrument on board the BepiColombo MMO will allow detailed identification of the material of planetary origin and its propagation, hence providing unprecedented information on the ionized environment of Mercury. The present paper is not intended to be the definitive paper on MSA. Its purpose is to present an expanded description of the instrument and to provide a partial summary of its performances through calibration data.

2. MSA Energy Analyzer

In contrast to the terrestrial environment where planetary material is essentially made of H^+, O^+, and He^+, a wide variety of species (e.g., H^+, He^{2+}, He^+, O^+, Na^+, Mg^+, K^+, and Ca^+) of planetary origin is likely in the environment of Mercury as a result of a variety of interaction processes with the planet surface (solar wind sputtering, micrometeoritic bombardment, thermal desorption…). For an improved characterization of these different ion species, an analyzer with enhanced mass resolution capability is thus necessary. In this respect, the FIPS analyzer on board the MESSENGER only allowed for moderate mass resolution, as evidenced for instance from Figure 1 or *Zurbuchen et al*. [2008]. In subsequent papers based on FIPS measurements [e.g., *Raines et al*., 2013], this lead to a classification of ions according to distinct groups of mass-to-charge ratios (viz., m/q between 16 and 20 amu/e for the so-called O^+ group and between 21 and 30 amu/e for the so-called Na^+ group). On board the BepiColombo MMO spacecraft, ion measurements with higher mass resolution will be obtained using the MSA instrument.

As illustrated in Figure 2, MSA features two main parts: (1) entrance and electrostatic analyzer (ESA) and (2) time-of-Flight (TOF) chamber. It exhibits a quite specific design for the time-of-flight analysis with a linear electric field (LEF) that leads to nearly isochronous TOFs, hence an enhanced mass resolution. Such an

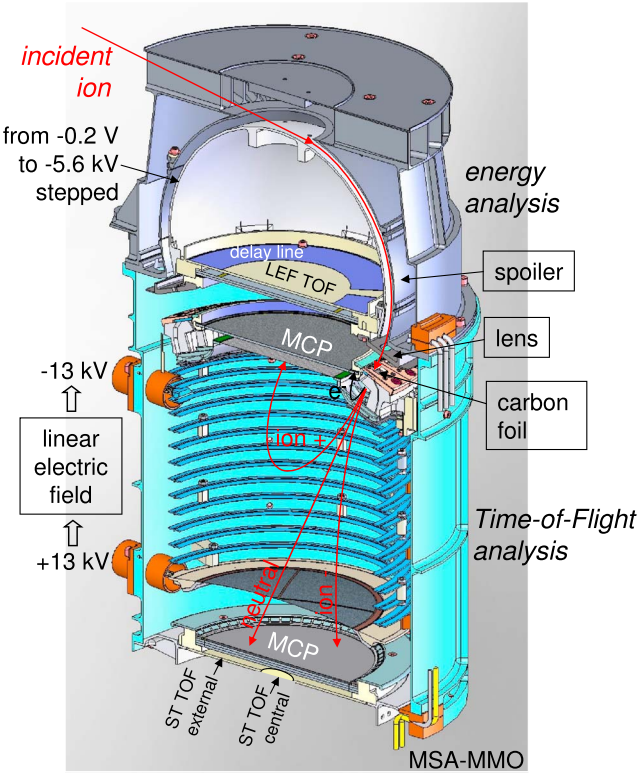

Figure 2. Schematic illustration of MSA principle of operation (adapted from *Delcourt et al.* [2009]).

instrumental design to characterize plasma composition is fairly unique and has been flown only on the JAXA Kaguya mission (MAP-PACE instrument) and on the NASA Cassini mission (Cassini Plasma Spectrometer–ion mass spectrometer (CAPS-IMS) instrument from which the MSA spectrometer derives [*Young et al.*, 2004]). MSA measurements will combine both enhanced mass resolution and three-dimensional distributions with high temporal resolution (8 s), and they will thus provide detailed information on ion populations at Mercury. This will allow us to progress toward a new understanding of plasma processes in this miniature magnetosphere.

Looking first at the instrument energy analyzer, it can be seen in Figure 2 that thin partition walls at MSA entrance define 32 windows of 11.25° in azimuth. As illustrated in Figure 3, seven of these entrance windows are blind (blue labels in Figure 3) due to the presence of MMO magnetometer mast, while four other windows are closed for mechanical clearance for support structures (red labels in Figure 3). This leaves 21 useful windows through which the ions enter the spectrometer (note that these entrance windows as well as energy analyzer electrodes downstream have been blackened

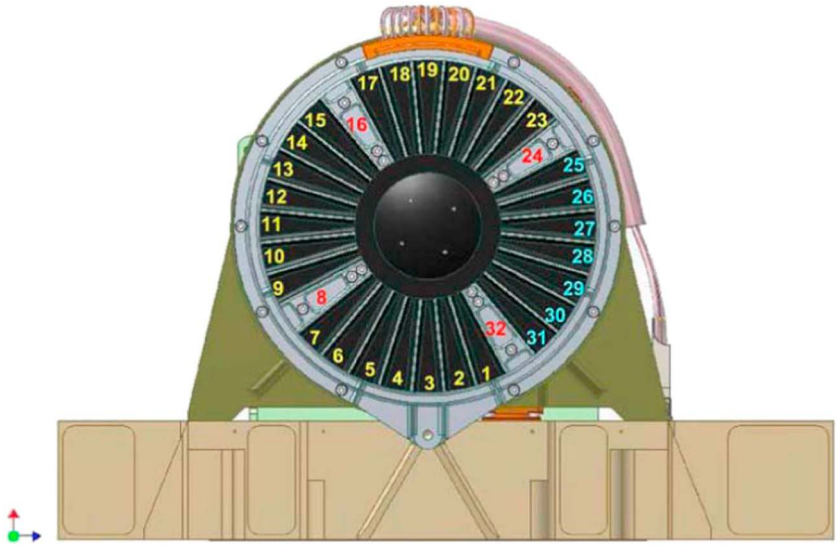

Figure 3. Side view of MSA entrance windows. Color-coded numbers correspond to the valid windows (in yellow), windows that are closed for mechanical purpose (in red), or windows that are closed due to MMO magnetometer mast (in blue). In the following, entrance window azimuth is measured clockwise with an origin placed at the center of window no. 11 that will point toward the Sun once per spin.

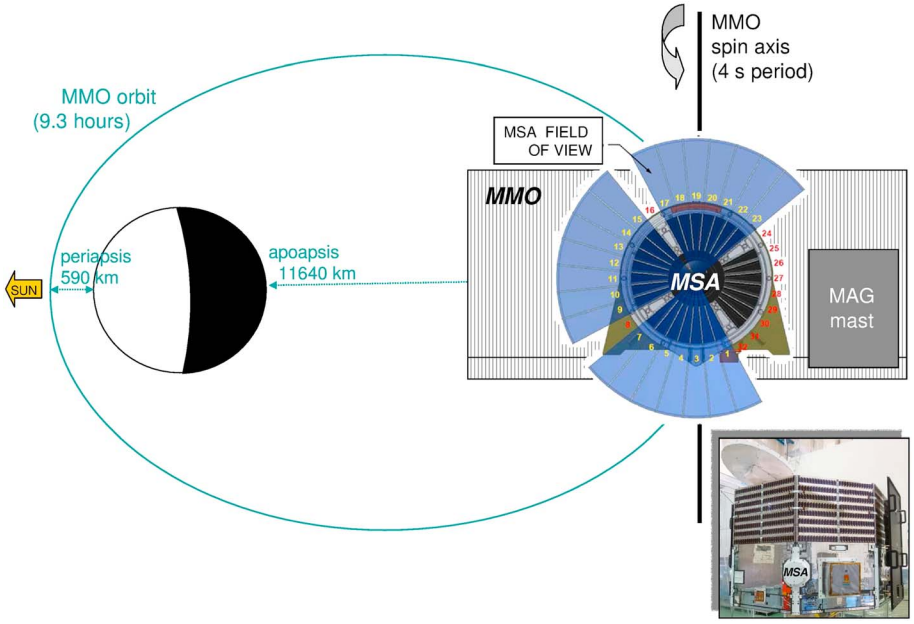

Figure 4. Schematic representation of MSA installation (not to scale) on the spacecraft and of its field of view (in blue) along MMO polar orbit. The insert at bottom right shows the MSA with its white thermal shield installed on the MMO spacecraft.

with copper sulfide to minimize UV pollution that can lead to noise and artificial counts). Since MMO is spin stabilized with spin axis perpendicular to the ecliptic plane, the solar wind will be recorded in the same MSA entrance windows (labeled 10, 11, and 12) throughout the spacecraft polar orbit, as is illustrated in Figure 4. This latter figure also illustrates how the magnetometer mast is constraining MSA field of view, measurements of the full 3-D ion distribution functions being obtained after one spacecraft spin (4 s).

Downstream of MSA entrance windows, ions travel through a spherical ESA that has its external electrode at ground potential (see Figure 2). The voltage applied to ESA inner electrode (up to a maximum value of −5.6 kV) allows to select specific energy per charge ratio. This can be better appreciated in Figure 5 that shows the voltage applied to the inner electrode for a 2 keV N^+ beam at entrance. It can be seen in Figure 5 that the voltage midpoint value is ~ −292 V on the average, yielding an analyzer constant *k* of

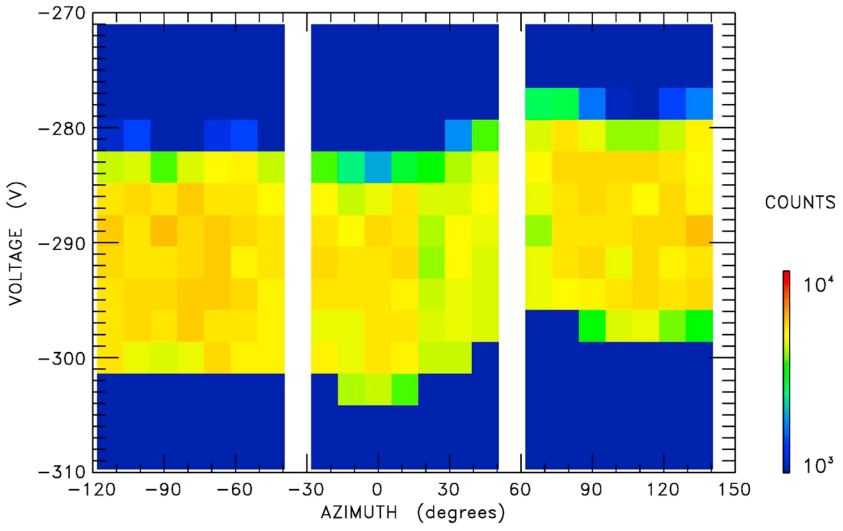

Figure 5. Voltage applied on the energy analyzer inner electrode versus entrance window azimuth (see Figure 3) for a 2 keV N^+ beam. Counts are coded according to the color scale at right.

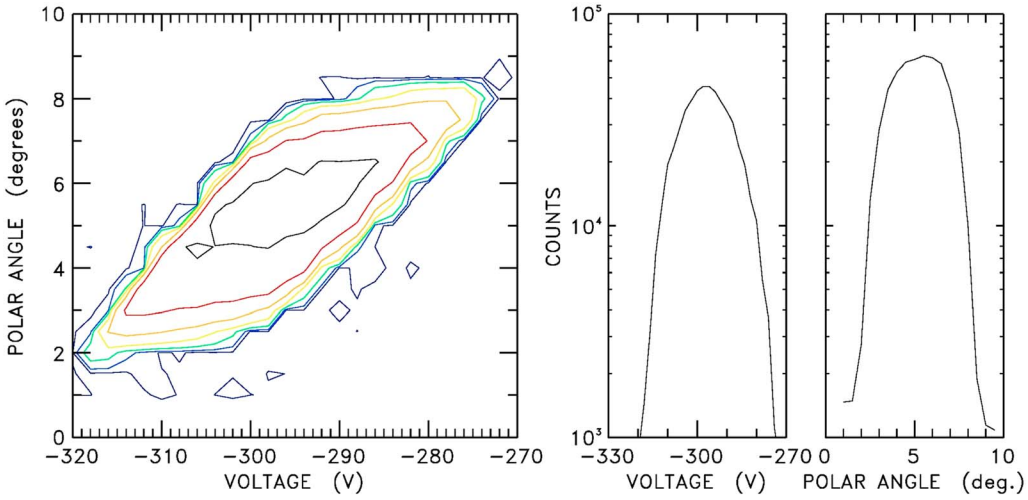

Figure 6. (left) Count rate contours as a function of polar angle (elevation) and voltage (energy) for entrance window no. 11 and using a 2 keV N^+ beam. (right) Integrated counts versus voltage and integrated counts versus polar angle.

~6.85. With a maximum voltage value of −5.6 kV, MSA can thus operate over a large range of energies, from a few eV/q up to ~38 keV/q. Further characteristics of the energy analyzer can be obtained from Figure 6 that shows contours of ion count rate versus polar angle and inner electrode voltage for one of the entrance windows (window no. 11). The full width at half maximum (FWHM) obtained in the middle plot is ~25 V, hence an energy resolution of ~8.5%. Also, in the rightmost plot of Figure 6, the polar angle (equivalently, elevation) midpoint value is ~5° with a FWHM of ~4.9°. MSA instantaneous field of view thus is ~5° × 260°. Finally, Figure 7 shows the count rate variation in one of the entrance windows (window no. 3) for a higher resolution in azimuthal angle. Like for other measurements shown in this paper, note here that the beam is fixed while the instrument rotates in front of this beam. The effect of partition walls regularly spaced by steps of 11.25° (see Figure 3) can clearly be seen in this figure with high count rate at the window center and decrease on either side. Note the slight asymmetry in this figure with respect to 0° azimuth, which may follow from either

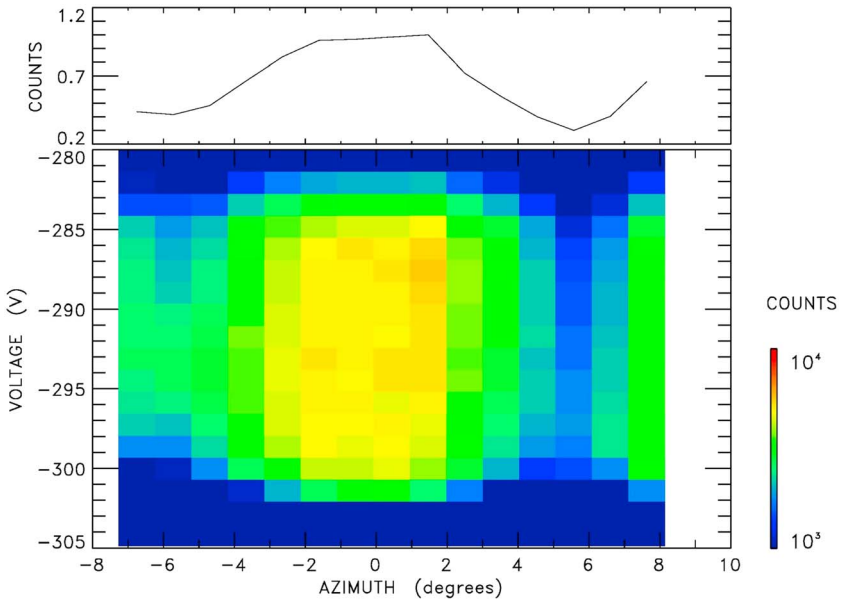

Figure 7. (top) Normalized integrated count rate as a function of azimuth. (bottom) Voltage applied on the energy analyzer inner electrode versus azimuth within entrance window no. 3 for a 2 keV N^+ beam. Counts are coded according to the color scale at right.

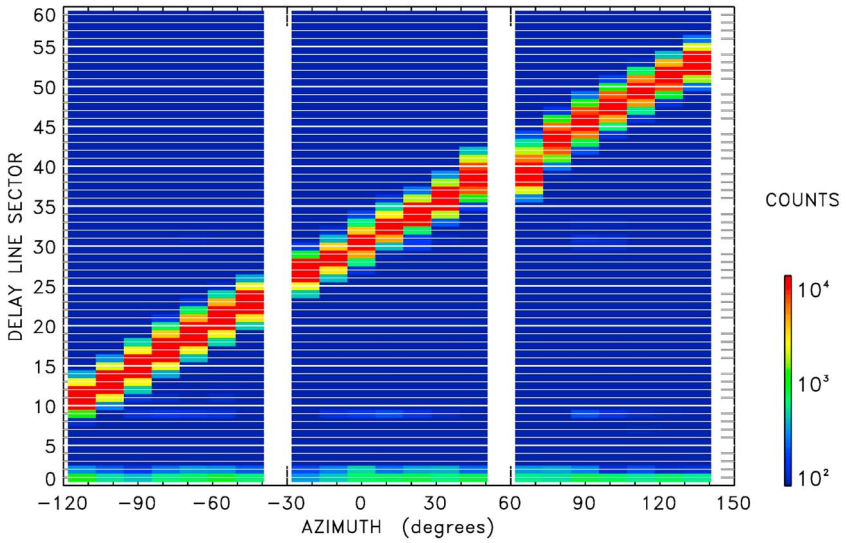

Figure 8. Delay line sector versus entrance window azimuth (see Figure 3). Counts are coded according to the color scale at right.

carbon foil inhomogeneity within this entrance window or from inhomogeneity of the N^+ beam that has a diameter of 20 mm (note that the beam itself was found to be fairly stable before and after this run).

In order to reduce the instrument geometrical factor when MMO will be in the solar wind or in the magnetosheath, a spoiler design has been implemented. That is, the ESA outer electrode has been divided into two parts (see Figure 2), and one of these parts can be independently polarized up to −300 V, leading to weaker electric field inside ESA. Such a spoiler voltage effectively alters the ion paths within ESA up to 2 keV/q, hence a reduction of the ion flux entering the instrument that has been defined with the help of numerical simulations. In practice, when the count rate over one spin exceeds 10^3 START events in one energy bin and one optic window, the spoiler voltage is increased by one step at the end of this spin, yielding lower analyzer efficiency (note that, on the opposite, when the count rate drops below 5×10^2, the spoiler voltage is decreased by one step and that, at the first switch-on, the spoiler voltage used is that corresponding to 10% efficiency to effectively reduce microchannel plate (MCP) saturation). Subsequently, the spoiler voltage is further increased (decreased) if the flux is too high (too low). For given spoiler voltage (i.e., given flux reduction at nominal E/q_{nom}), the ion flux at energies smaller (larger) than E/q_{nom} is damped (unchanged). Finally, the spoiler itself has been segmented in such a way that the geometrical factor can be reduced only in the solar wind direction (viz., windows 10-11-12 in Figure 3), which leaves full MSA capability in other directions or in all directions (e.g., to measure large ion fluxes in the magnetosheath).

3. MSA Time-of-Flight Analyzer

At exit of the energy analyzer, ions are accelerated toward the entrance of the TOF analyzer (see Figure 2) that is polarized at a very high voltage VHV_1 that has a maximum value of −13 kV. Note that an intermediate electrode (referred to as lens in Figure 2) polarized at 1 kV is located close to the exit of the ESA in order to prevent the large accelerating electric field to penetrate deep into the ESA and have a detrimental effect on the ion trajectories and ESA performances. At entrance of the TOF analyzer and for each of the 21 optic windows, ions impact thin (~1 $\mu g/cm^2$) carbon foils. As a result of this impact, the carbon foils emit one or several secondary electrons in the forward direction [e.g., *Allegrini et al.*, 2003; *Funsten et al.*, 2005]. These secondary electrons are deflected and focused by a dedicated electrostatic optics toward the outer part of the top MCP (see Figure 2), as featured in *Moebius et al.* [1990] (see, e.g., Figure 1 of that paper). Downstream of this MCP outer part, electrons are collected on a delay line (shown in purple in Figure 2 [see *Saito and Yokota*, 2016]). The position of the electron impact on this delay line allows us to identify the azimuthal sector of the incoming ions.

This can be better appreciated in Figure 8 that shows the mapping obtained between delay line sectors and the 21 azimuthal channels (entrance windows). Measurements of the START rate in these distinct channels

Table 1. Characteristics of Nominal TOF Mode (i.e., TOF Events Have One STOP for Each START)[a]

MMO spin period	4 s	S
Number of sectors per spin	32	N
Spin sector duration	125 ms	$T = S/N$
Number of energy steps per spin sector	32	n
Energy step duration	3.9 ms	$t = T/n$
TDC resolution	0.78125 ns	R
Size of fixed TOF window	1562.5 ns	$W = 2000 \times R$
Maximum number of counts per energy step	2496	$C = t/W$
LEF TOF of Fe^+ ions	~1460 ns (8 kV) ~1245 ns (11 kV)	

[a]LEF TOFs of Fe^+ ions for two different VHV_1 (8 and 11 kV) also are indicated for reference.

yield the three-dimensional angular and energy distributions without mass identification on the time scale of the spin period (4 s). Note in Figure 8 that the different entrance windows of MSA gradually spread over the different delay line sectors as they should. Some of the delay line sectors (<9 or >56) correspond to MSA windows that are closed due to magnetometer mast (see Figure 3) and could be used for radiation monitoring. In practice, however, these latter angular domains will not be transmitted within MSA mission data. For some other delay line sectors (e.g., sector 20 or sector 40), there exists an ambiguity to associate these sectors with a given entrance window or the neighboring one. Sector allocation here was based on comparable weighing within the different entrance windows. This may result in the end into some angular uncertainties to define the direction of propagation of ions, an uncertainty that amounts to two entrance windows (viz., $2 \times 11.25°$). Still, as will be discussed hereinafter (see section 4), MSA mission data in most observation modes will be reduced to 36 directions of view per spin due to telemetry constraints. The above uncertainty may be relevant only in the high spatial mode of observation, where the maximum angular resolution of the instrument will be used. Finally, note in Figure 8 the slight increase in the net count rate as azimuth is increasing. This evolution that differs from that observed in Figure 5 likely follows from the beam variation during the runs.

The START pulse obtained from the secondary-electron impact is used to initiate TOF measurement. The nominal MSA mode for TOF measurement has one STOP for each START. That is, the START pulse produced by the secondary electron is used to open a TOF window, during which a STOP pulse is expected. As summarized in Table 1, this TOF window has a fixed size of 1562 ns, which allows us to measure heavy ions on the LEF detector up to $m/q \approx 60$ at $VHV_1 = -8$ kV (and up to larger m/q at $VHV_1 = -11$ kV). Note that the time-to-digital converter resolution to measure these TOFs is 0.78125 ns. In addition to this nominal TOF mode, another TOF mode can be activated that allows up to three STOPs per START signal. This mode has been implemented to track molecular ions. These molecules can be identified from the times of flight of their daughter products that are produced downstream of the carbon foils, as described in equation (2) of *Gilbert et al*. [2010].

Upon interaction with the carbon foils, the incoming ions may be subjected to angular and energy diffusion that depends upon ion mass and energy. Also, as a result of charge exchange, ions may exit the carbon foils as neutrals, positive, or negative ions. Here a "reflectron" principle [*Managadze*, 1986] is used to increase the mass resolution for positive ions. Specifically, instead of an equipotential TOF chamber like in the MESSENGER FIPS instrument, an electric field is applied inside the TOF chamber that varies nearly linearly with distance along the instrument main axis (referred to as z direction in the following), from -13 kV (maximum voltage) at the carbon foil level up to +13 kV (maximum voltage) at the gridded electrode near the bottom end of the TOF chamber. The effect of this linear electric field (LEF) is to reflect positive ions toward the top of the TOF chamber (see Figure 2). The use of a LEF allows us to minimize the energy and angular aberrations in the time of flight of these reflected ions. Indeed, in the case of particles traveling only in the z direction, the equation of motion is that of a simple harmonic oscillator of mass m:

$$md^2Z/dt^2 = qE = -qCZ \tag{1}$$

where C is a constant describing the electric field variation. After solving equation (1), one obtains the following relationship between the mass-to-charge ratio of a given ion and its time of flight [see, e.g., *McComas et al*., 1990]:

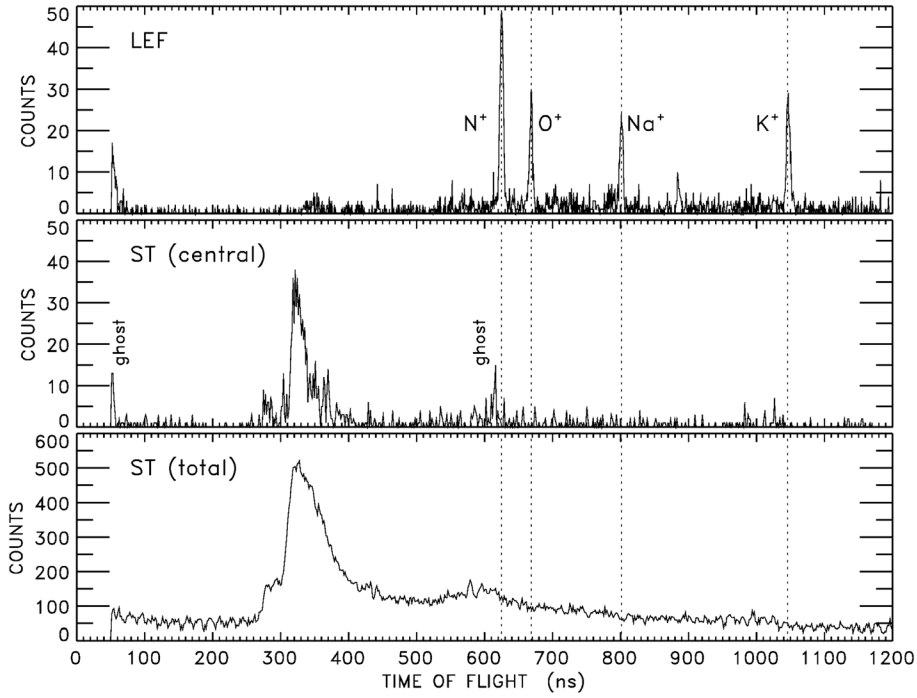

Figure 9. TOF spectra for a 5 keV beam of different ion species (N^+, O^+, Na^+, and K^+): (top) LEF, (middle) ST central, and (bottom) ST external added to ST central (see Figure 2). The high voltage applied to the TOF chamber is 11 kV.

$$m/q = CT^2/\pi^2 \tag{2}$$

It can be seen in equation (2) that the particle time of flight T depends neither upon energy nor angle at entry into the TOF chamber (isochronous TOF). As a result, narrow TOF spectra are obtained, hence an enhanced mass resolution. Note here that only positive ions with an energy at MSA entrance less than 13 kV (maximum voltage) may be reflected by the LEF and detected on the central part of the top detector that provides the STOP signal (see Figure 2).

The top plot of Figure 9 shows an example of LEF TOF spectra obtained for a variety of ion species that were available for MSA calibration in Institute of Space and Astronautical Science (ISAS) vacuum chamber (N^+, O^+, Na^+, and K^+). Note that the very high voltage used here is 11 kV and that the spectra were recorded using MSA flight electronics with TOF resolution of 0.78125 ns (see Table 1). Although K^+ ions are subjected to larger angular and energy diffusion than N^+ upon interaction with the carbon foils, the top plot of Figure 9 clearly demonstrates that narrow TOF spectra are obtained regardless of ion species. Although ions do not travel exactly along the z direction, it is also apparent from this plot that TOFs are organized according to equation (2), with a C parameter on the order of 3.7×10^6 MKSA. This gives times of flight of ~624 ns, ~667 ns, ~800 ns, and ~1041 ns for N^+, O^+, Na^+, and K^+ ions, respectively, in Figure 9. Conversely, equation (2) allows us to readily derive the m/q ratio from given time of flight T, hence the ion mass with a very good resolution ($m/\Delta m \approx 40$).

On the other hand, the largest fraction (~80%) of incoming particles exits the carbon foil as neutrals or negative ions. These particles have “straight through" (ST) trajectories toward the bottom end of MSA TOF chamber, where the STOP signal is measured (see Figure 2). Note that this is also the case for positive ions that have energies larger than 13 keV (maximum value) at entrance of the instrument and that are not reflected by the LEF. In this latter case, like other spectrometers with equipotential TOF chamber (e.g., MESSENGER FIPS), the TOFs obtained display prominent spreading due to angular and energy diffusion upon interaction with the carbon foils. Here the TOF obtained for neutrals is of the form:

$$m/q = 2(E/q)T^2/L^2 \tag{3}$$

where E is the energy at entrance of the TOF chamber and L is the distance traveled within the TOF chamber. Because of TOF spread, the ST resolution is significantly smaller than that of LEF. Still, to improve this resolution,

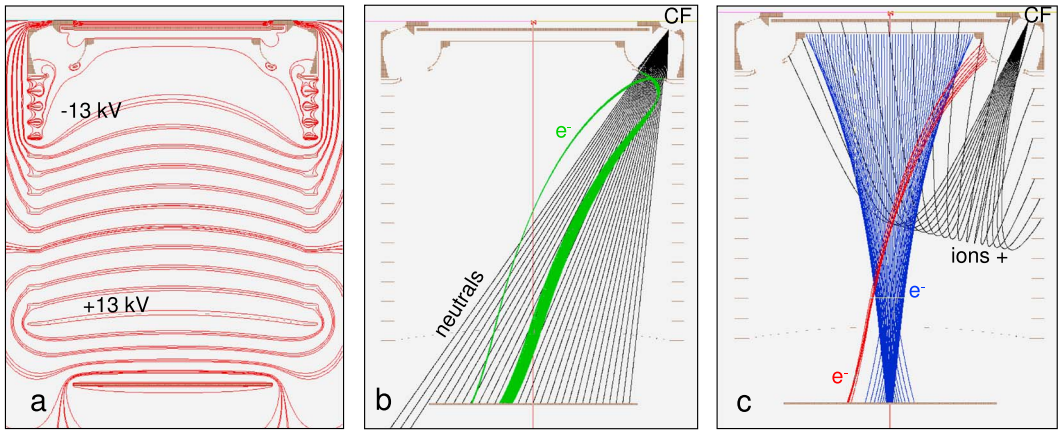

Figure 10. (a) Equipotential contours (in red) within MSA TOF chamber. (b) Model trajectories of neutrals (in black) and electrons emitted at exit of the deflection box (in green). (c) Model trajectories of reflected positive ions (in black) and electrons emitted from the edge of the deflection box (in red) or from the grid upstream of the LEF detector (in blue). Trajectories coded in green, blue, and red in this figure show the selected examples of secondary-electron trajectories that cause ghost peaks in Figure 9.

the MSA ST detector has been divided into two parts: a small central disk (~14 mm in diameter) and a large outer ring (see Figure 2). Particles collected on the central disk have a reduced spread in path length (*L* parameter in equation (3)) as well as in energy since they enter the TOF chamber in the direction nearly normal to the carbon foils. As compared to this central part, the outer ring has a larger useful surface (thus, a larger count rate) but also a larger spread in the length of ion trajectories and in ion energy, hence a reduced mass resolution.

This can be appreciated in the middle and bottom plots of Figure 9 that show the TOF spectra obtained for central ST and total ST, respectively. It should be stressed here that the test conditions are identical to those in the top plot of Figure 9, viz., N^+, O^+, Na^+, and K^+ ions with a TOF chamber high voltage of 11 kV. The TOF spectra obtained here sharply contrast with the narrow LEF spectra discussed above (top plot of Figure 9) and are more comparable to those of MESSENGER FIPS (see, e.g., Figure 1 of *Zurbuchen et al.* [2008]). As expected, the count rate for central ST (middle plot) is significantly smaller than that of total ST (bottom plot), but a somewhat larger mass resolution is obtained (typically, $m/\Delta m \approx 10$ for ST central as opposed to $m/\Delta m \approx 5$ for ST total). In the bottom plot of Figure 9, note also that because of the large angular and energy diffusion experienced upon interaction with the carbon foils, heavy ions (e.g., K^+) have large TOF spectra that are not clearly identified in the long TOF tail. During MSA operations, since these heavy ions cannot be unambiguously identified, groups of ions (e.g., O^+ group, Na^+ group, and K^+ group) will be defined for selected intervals of ST times of flight, in a like manner to FIPS data [e.g., *Raines et al.*, 2013].

In the middle plot of Figure 9, some narrow ghost peaks are noticeable. One of these ghost peaks occurs near 610 ns, immediately before the N^+ LEF TOF. To illustrate the origin of this peak, Figure 10 shows the examples of secondary-electron trajectories within MSA TOF chamber, using arbitrary initial parameters. It is apparent from the trajectories in blue in the right plot of Figure 10 that secondary electrons emitted upon impact of N^+ ions on the grid (80% transparency) located upstream of the LEF MCP are rapidly accelerated downward, due to the potential configuration inside MSA TOF chamber (left plot of Figure 10). After downward acceleration, these secondary electrons are recorded on the ST detector a few nanoseconds before the ion detection on LEF (top plot of Figure 9), hence the above ghost peak. Secondary electrons emitted from the electron deflector (trajectories in red in the right plot of Figure 10) may also contribute to some ghost peaks a few tens of nanoseconds before the LEF ion detection. In the middle plot of Figure 9, another ghost peak is noticeable near 50 ns. As illustrated in the middle plot of Figure 10, this latter ghost peak is due to secondary electrons emitted at exit of the electron deflector (trajectories in green). The times of flight of these secondary electrons correspond to that of ions within the electron deflector plus ~10 ns needed to travel from top to bottom inside MSA TOF chamber. The larger the diffusion upon interaction with the carbon foil is (e.g., for heavier ions or for lower energies), the more intense this ghost peak is. Although artificial, these two types of ghost

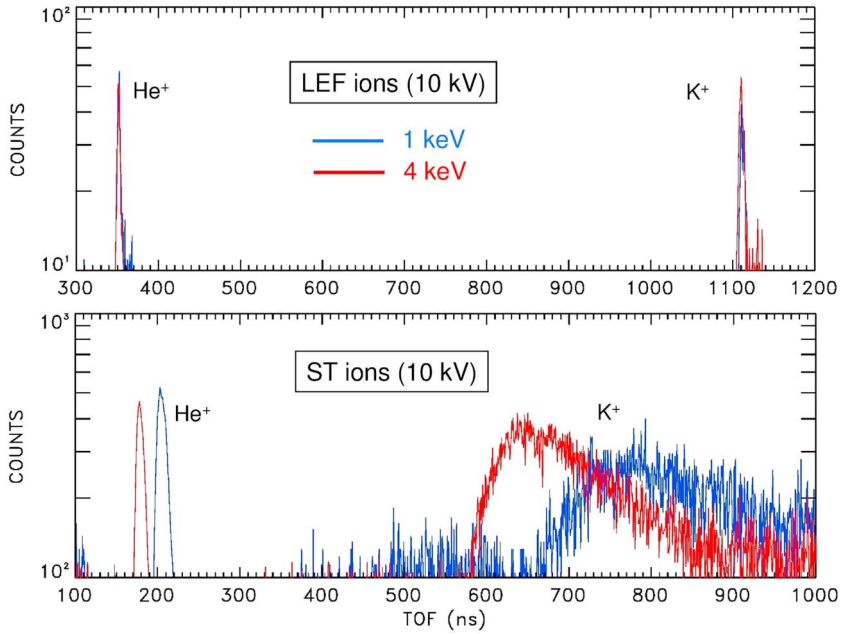

Figure 11. (top) LEF and (bottom) ST total TOF spectra obtained for ion species at the two ends of the mass scale (viz., He^+ and K^+) and for two different energies: 1 keV (shown in blue) and 4 keV (shown in red). The high voltage applied to the TOF chamber is 10 kV. Note that different scales are used in abscissa in the top and bottom plots.

peaks are obtained within specific TOF ranges and thus are not an issue for MSA operation. Finally, in the top plot of Figure 9, a peak is also observed near 60 ns. This latter feature does not result from secondary-electron emission but is likely due to MCP cleanliness. It was found to decrease with time during MSA calibration.

To complement the results shown in Figure 9, results of additional beam tests are shown in Figure 11 for different ion species (He^+ and K^+) and different energies (1 keV and 4 keV). This latter figure clearly exemplifies the above discussed properties of LEF and ST TOF spectra. Indeed, the top plot of Figure 11 that displays LEF data reveals that TOF spectra obtained at different energies approximately overlap. That is, the median TOF for He^+ ions is ~353 ns at 4 keV and ~354 ns at 1 keV with FWHM of ~7 ns. Also, this median TOF is on the order of 1110 ns for K^+ ions at both 1 keV and 4 keV (with a FWHM of ~10 ns). In other words, regardless of ion energy, nearly identical TOFs are obtained for given ion species, as expected from the isochronous character of LEF data (see equation (2)). The bottom plot of Figure 11 that displays ST total measurements shows a different situation with no overlap of TOF spectra. Here the median TOF is ~180 ns and ~206 ns for He^+ ions with 4 keV and 1 keV energy at entrance, respectively (with FWHM of ~15 ns). This median TOF becomes on the order of 671 ns and 713 ns for 4 keV and 1 keV K^+ ions, respectively (with FWHM of ~170 ns). In other words, ST spectra are not isochronous and the TOF values obtained are increasing with decreasing ion energy, as expected from equation (3).

To better understand the response of the instrument, an electrooptic model of MSA has been developed, which uses TRIM simulations to characterize the ion interaction with the carbon foils. This numerical model proved to be useful during instrument calibration, and it will be used for MSA data analysis as a noise-mitigating technique as well. Figure 12 shows an example of the TOF spectra obtained with this numerical model. Here different ion species were considered with a TOF chamber high voltage of 11 kV. It can be seen that narrow LEF TOF spectra are obtained, which are consistent with those obtained experimentally (see top plot of Figure 9). As for ST spectra, the comparison of middle and bottom plots of Figure 12 clearly exemplifies the better resolution obtained using the small central disk of the ST detector (middle plot) instead of the full ST. Particles collected on this central disk have a reduced spread in path length (L parameter in equation (3)) as well as in energy so that the corresponding TOF spectra are narrower than those obtained for ST total (bottom plot of Figure 12). This is at the expense of count rate that is significantly smaller on ST central than on ST total.

Because the detection surface of ST total is larger than that of ST central (i.e., larger variation in path length L in equation (3)), a widening of the spectra is obtained in the bottom plot of Figure 12, with TOFs substantially smaller or larger than the median one. As discussed in Figure 9, long tails also are noticeable for heavy ions in

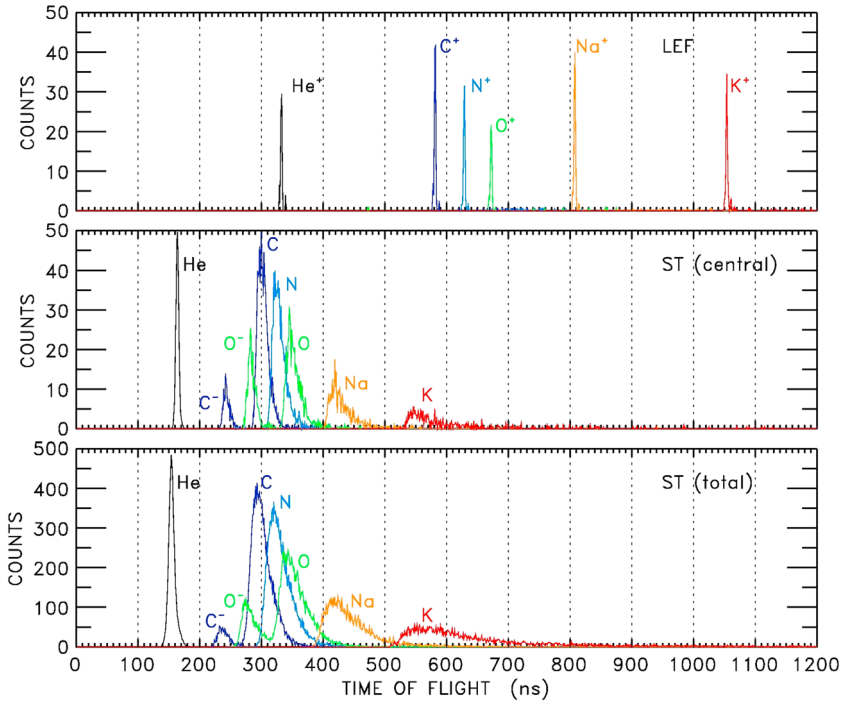

Figure 12. Simulated TOF spectra obtained with an electrooptic model of MSA: (top) LEF, (middle) ST central, and (bottom) ST external added to ST central (like in Figure 9). Different (color-coded) ion species (He^+, C^+, N^+, O^+, Na^+, and K^+) with 4 keV energy at MSA entrance are considered. The high voltage applied to the TOF chamber is 11 kV. Note the different scales in ordinate in the top plots as compared to the bottom plot due to larger count rates on ST total.

the bottom plot of Figure 12, which is not the case for light ions. This is due to a more pronounced angular diffusion and energy straggling of heavy ions during crossing of the carbon foils. These long tails somewhat weaken in ST central spectra (middle plot of Figure 12) since the particles collected here are those traveling essentially in the direction normal to the carbon foils. In both ST central and ST total spectra of Figure 12, note moreover the additional peaks obtained for C and O particles that are due to electron capture upon interaction with the carbon foil, hence downstream beams that contain not only neutrals but also negative ions (C^- and O^-). These negative ions are accelerated toward the ST detector by the linear electric field (see Figure 2), giving spectra at somewhat smaller TOF values than those of neutral particles. Altogether, the combination of N, O, Na, and K spectra in the bottom plot of Figure 12 can be used to effectively reconstruct the overall TOF profile obtained experimentally in the bottom plot of Figure 9.

As reported in previous studies [e.g., *Young et al*., 2004; *Gilbert et al*., 2014], time-of-flight measurements to derive the ion m/q may come together with artificial counts or spurious signals, due to a variety of secondary-electron emissions or UV contamination. The ghosts noticeable in Figure 9 are just an example of such signals. As far as UV is concerned, special care was taken to prevent UV reflections within MSA energy analyzer that can lead to noise inside the TOF chamber. The azimuthal partition walls at MSA entrance already provide a good protection to reduce the UV flux penetrating into the instrument. In addition, MSA entrance and ESA parameters (maximum height and length of partition walls, distance between inner and outer electrodes, and opening angle) were optimized to ensure at least three reflections along a UV path inside the energy analyzer. This together with copper sulfide blackening of the different parts of the ESA and of the entrance section minimize UV pollution at entry of the TOF chamber. Also, as mentioned above, it should be pointed out that a dedicated electrostatic optics was implemented in MSA TOF chamber to deflect secondary electrons emitted by the carbon foils toward the top MCP (see Figure 2). As compared to Cassini CAPS-IMS, which MSA derives from and where secondary electrons were detected on the bottom MCP (see, e.g., Figure 3 of *Young et al*. [2004]), this ensures cleaner detection of START signals. Note that these secondary-electron deflectors may lead to artificial counts as well but in a well-identified TOF range (see trajectories in green in Figure 10). More generally, note also that the use of double coincidences (i.e., both START and STOP detectors are triggered for a measurement to be valid) in such TOF instruments effectively helps

Table 2. Summary of MSA Performances

Field of View	5° × 260°
Angular resolution	5° × 11.25°
Energy range	1 eV/q–38 keV/q
Energy resolution	8%
Mass range	1–60 amu
Mass resolution	$m/\Delta m = 10$ $m/\Delta m = 40$ (for LEF ions <13 keV/q)
Time resolution	3-D distribution function in 4 s (32 energy steps) 3-D distribution function in 8 s (64 energy steps)
G factor (cm^2 sr eV/eV; 21 windows)	7×10^{-3} (ST); 5×10^{-4} (LEF)

reduce the noise that may be present in the measurements (see, e.g., Figure 3 of *Gilbert et al*. [2014]). Finally, while in orbit at Mercury, the electrooptic model of MSA (see Figure 12 above) will be used to corroborate the measured TOF spectra and help mitigate noise effects.

4. MSA Development

Table 2 summarizes the MSA performances described above. Also, the top plot of Figure 13 shows a view of the flight model of the instrument that was delivered to the MMO spacecraft in June 2014. The dimensions of the instrument are 325 mm × 287 mm × 232 mm. Mass and power in medium telemetry mode are ~4.46 kg and ~9.1 W, respectively, which yield a power-to-mass ratio of ~2 that is fairly standard for such a mass spectrometer on a spinning spacecraft. The MSA instrument that has a geometric factor of 7×10^{-3} cm^2 sr eV/eV for the ST part (i.e., about 7 times larger than that of MESSENGER FIPS) will be operating over a large range of energies, from a few eV/q up to ~38 keV/q, using two interleaved voltage tables from one spin to another to ensure a better coverage of the whole energy range. This will allow us to obtain three-dimensional distribution functions in 4 s (32 energy steps) or 8 s (64 energy steps). MSA mission data will include two types of matrices: (1) TOF matrices obtained from both LEF data (weak efficiency but high mass resolution) and ST data (moderate mass resolution but high count rates) and (2) count rate matrices that will be obtained after binning ST data according to fixed (energy-TOF dependent) mass groups. Both types of matrices will be downlinked with energy, angular, and temporal resolutions that will depend upon the observation mode that is selected (viz., survey, high spatial resolution, and high temporal resolution). Specifically, although count rate

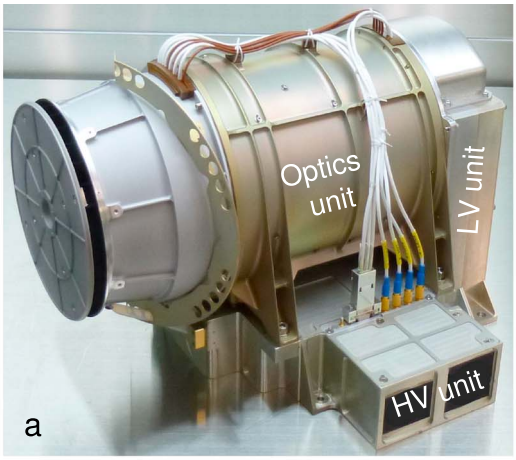

Figure 13. (a) MSA flight model (ISAS; June 2014) and (b) MSA block diagram. Optic unit was provided by LPP, HV unit by MPS, DPU by IDA, and AMPSW by ISAS. Pink arrows show the command or data flow directions. Abbreviations stand for linear electric field (LEF), straight through (ST), medium voltage (MV), very high voltage (VHV), high voltage (HV), low voltage (LV), data processing unit (DPU), telemetry (TM), telecommand (TC), amplifier board (Amp), and SpaceWire (SW).

matrices internally have a high angular definition (typically, 21 anodes of 11.25° × 32° spin sectors of 11.25°), telemetry constraints impose to reduce these count rate matrices to 36 directions of view per spin, except when the high spatial resolution mode of observation will be used.

The MSA instrument was developed in the frame of an international collaboration between four distinct laboratories, viz., (1) ISAS, Sagamihara, Japan (MSA PI: Y. Saito), which was in charge of MSA amplifier board and interface with MMO; (2) LPP, Paris, France (MSA co-PI: D. Delcourt), which was in charge of MSA electrostatic optics; (3) MPS, Göttingen, Germany, which was in charge of MSA high-voltage power supplies; and (4) IDA, Braunschweig, Germany, which was in charge of MSA central processing unit. A block diagram describing these four distinct subunits is shown in the bottom plot of Figure 13. After development in the different laboratories, MSA assembling, tests, and calibration were performed at ISAS-JAXA.

5. Summary

Following the pioneering observations of the NASA MESSENGER mission, the MMO spacecraft of the ESA-JAXA BepiColombo mission will be dedicated to comprehensive investigations of Mercury's magnetosphere. On board this spacecraft, the MSA ion spectrometer that is part of the MPPE suite of particle instruments (PI: Y. Saito) will measure three-dimensional distributions in the ~1 eV–38 keV range with unprecedented mass resolution. Here the use of an improved reflectron technique in the time-of-flight chamber that has been seldom flown on planetary missions will allow us to unambiguously distinguish between neighboring mass-to-charge ratios, hence new possibilities in understanding the coupling between the planet surface and its environment. Simultaneously, MSA will provide three-dimensional measurements with lesser mass resolution but with higher sensitivity that will allow us a new and thorough characterization of Mercury's plasma environment.

Acknowledgments
The data that are used in this paper and that are shown in figures and table are available from first author (dominique.delcourt@lpp.polytechnique.fr) upon request. Data that are referred to in this paper are available in cited references.

References

Allegrini, F., R. F. Wimmer-Schweingruber, P. Wurz, and P. Boschler (2003), Determination of low-energy ion induced electron yields from thin carbon foils, *Nucl. Instrum. Meth. Phys. Res. B*, *211*, 487.

Anderson, B. J., M. J. Acuna, D. A. Lohr, J. Scheifele, A. Raval, H. Korth, and J. A. Slavin (2007), The magnetometer instrument on MESSENGER, *Space Sci. Rev.*, *131*, 417.

Anderson, B. J., et al. (2011), The global magnetic field of Mercury from MESSENGER orbital observations, *Science*, *333*, 1859, doi:10.1126/science.1211001.

Andrews, G. B., et al. (2007), The energetic particle and plasma spectrometer instrument onboard the MESSENGER spacecraft, *Space Sci. Rev.*, *131*, 523.

Delcourt, D. C. (2013), On the supply of heavy planetary material to the magnetotail of Mercury, *Ann. Geophys.*, *31*, 1673, doi:10.5194/angeo-31-1673-2013.

Delcourt, D. C., et al. (2009), The Mass Spectrum Analyzer onboard BepiColombo MMO: Scientific objectives and prototype results, *Adv. Space Res.*, *43*, 869, doi:10.1016/j.asr.2008.12.002.

Funsten, H. O., R. W. Harper, and D. J. McComas (2005), Absolute detection efficiency of space-based ion mass spectrometers and neutral atom imagers, *Rev. Sci. Instrum.*, *76*, doi:10.1063/1.1889465,053301.

Gilbert, J. A., R. A. Lundgren, M. H. Panning, S. Rogacki, and T. H. Zurbuchen (2010), An optimized three-dimensional linear electric field time of flight analyzer, *Rev. Sci. Instrum.*, *81*, doi:10.1063/1.3429941,053302.

Gilbert, J. A., D. J. Gershman, G. Gloeckler, R. A. Lundgren, T. H. Zurbuchen, T. M. Orlando, J. McLain, and R. von Steiger (2014), Characterization of background sources in space based time of flight mass spectrometers, *Rev. Sci. Instrum.*, *85*, doi:10.1063/1.4894694,091301.

Ho, G. C., et al. (2011), MESSENGER observations of transient bursts of energetic electrons in Mercury's magnetosphere, *Science*, *333*, 1865, doi:10.1126/science.1211141.

Managadze, G. G. (1986), Time of flight mass spectrometer, US patent 4611118, September 9 1986.

McComas, D. J., J. E. Nordholt, S. J. Bame, B. L. Barraclough, and J. T. Gosling (1990), Linear electric field mass analysis: A technique for three-dimensional high mass resolution space plasma composition measurements, *Proc. Natl. Acad. Sci. U.S.A.*, *87*, 5925.

Moebius, E., P. Bochsler, A. G. Ghielmetti, and D. C. Hamilton (1990), High mass resolution isochronous time-of-flight spectrograph for three-dimensional space plasma measurements, *Rev. Sci. Instrum.*, *61*, 3609, doi:10.1063/1.1141580.

Raines, J. M., et al. (2013), Distribution and compositional variations of plasma ions in Mercury's space environment: The first three Mercury years of MESSENGER observations, *J. Geophys. Res. Space Physics*, *118*, 1604–1619, doi:10.1029/2012JA018073.

Raines, J. M., et al. (2015), Plasma sources in planetary magnetospheres: Mercury, *Space Sci. Rev.*, doi:10.1007/s11214-015-0193-4.

Saito, Y., and S. Yokota (2016), High speed MCP anodes for high time resolution low energy charged particle spectrometers, this issue.

Saito, Y., J.-A. Sauvaud, M. Hirahara, S. Barabash, D. C. Delcourt, T. Takashima, K. Asamura, and BepiColombo MMO/MPPE team (2010), Scientific objectives and instrumentation of Mercury Plasma Particle Experiment (MPPE) onboard MMO, *Planet. Space Sci.*, *58*, 182.

Slavin, J.-A., et al. (2012), MESSENGER observations of a flux transfer event shower at Mercury, *J. Geophys. Res.*, *117*, A00M06, doi:10.1029/2012JA017926.

Sundberg, T., et al. (2012), MESSENGER observations of dipolarization events in Mercury's magnetotail, *J. Geophys. Res.*, *117*, A00M03, doi:10.1029/2012JA017756.

Young, D., et al. (2004), Cassini plasma spectrometer investigations, *Space Sci. Rev.*, *114*, 1, doi:10.1007/s11214-004-1406-4.

Zurbuchen, T. H., et al. (2008), MESSENGER observations of the composition of Mercury's ionized exosphere and plasma environment, *Science*, *321*, 90, doi:10.1126/science.1159314.

Zurbuchen, T. H., et al. (2011), MESSENGER observations of the spatial distribution of planetary ions near Mercury, *Science*, *333*, 1862, doi:10.1126/science.1211302.

Erratum

In the originally published version of this article, the description of the C parameter of equation (2) as it relates to Figure 9 contained the wrong exponent. It initially read "3.7×10^{-13}" but should read "3.7×10^{6}". The exponent has been corrected, and this version may be considered the authoritative version of record.